# Characterization of micro-anomalies *from* macro-scale response

Sourish Chakravarty* and Sonjoy Das†
*Mechanical and Aerospace Engineering, University at Buffalo, Buffalo, NY, 14260, USA*

**A stochastic multi-scale based approach is presented in this work to detect signatures of micro-anomalies *from* macro-level response variables. In this work, we particularly consider polycrystalline materials, e.g., Aluminium. Thus, by micro-anomalies, we refer to micro-cracks of size $10$–$100\ \mu\mathrm{m}$, while macro-level response variables imply, e.g., strains, strain energy density of macro-level structures of typical size often varying at the order of $10$–$100$ m (e.g., an aircraft wing). For different material and systems (e.g., sand and geo-mechanical systems), the sizes of micro- and macro- level scales may, of course, be significantly different. The micro-anomalies in the context of present work are not discernible by the naked eye. Nevertheless, they can cause catastrophic failures of structural systems due to fatigue cyclic loading that results in *initiation* of fatigue cracks. Analysis of such precursory state of internal damage evolution, before a macro-crack visibly appears (say, size of a few cms), is beyond the scope of conventional crack propagation analysis, e.g., fracture mechanics. The present work is proposed to address this specific concern, and is an extension of an earlier work by Das[2,3]. In the earlier work, macro-level (continuum) constitutive properties (e.g., constitutive elasticity tensors) of heterogeneous materials were constructed within a probabilistic formalism based on random matrix theory, maximum entropy principle, and principles of minimum complementary energy and minimum potential energy. The effects of micro-cracks are now incorporated into the present formulation by extending the previous work. Distinct differences are observed in the macro-level response characteristics depending on presence or absence of micro-cracks. Such stochastic information is used in the framework of optimization to detect the damaged region, consisting of microcracks, from experimentally obtained macroscale strain observations. Several schemes based on both heuristic and traditional optimization techniques are proposed and tested to detect damage due to microcracks depending on the availability of information. The proposed work is likely to be useful in health monitoring of structural systems in, but not limited to, aerospace, mechanical, and civil engineering applications.**

## I. Introduction

Analysis of structural systems characterized by multiple scales is a challenging task. Purely deterministic models or purely stochastic models dealing with such problems have their own drawbacks. The former results in point-estimates of model predictions that lack the capability of rigorously predicting scatters typically observed in experimental measurements, while the latter could violate certain governing physical laws that may be regarded as fundamental principles by the scientific community. A better approach would, therefore, be to adopt a physics-based stochastic approach that duly respects the fundamental principles of general deterministic formalism while accounting for the effects of scatters in predictions. The current work fits this niche.

In this work, a structural system of interest is conceptually envisaged as characterized by two distinct length scales: a *micro-scale* regime ($0.001$ mm to $1$ mm) which refers to the microstructure of polycrystalline materials (e.g., Aluminium) characterized by grain morphology, inclusions or cracks ($\sim 0.1$ mm), and a *macro-scale* regime ($>>$ 1mm) which alludes to the original structural system (e.g, an aircraft wing) that must be modeled by incorporating the effects of micro-structural information for the purpose of reliable prognosis. The micro-structural information is additionally presumed to be high-fidelity deterministic information which is available only in limited amount. This is practically consistent since it often takes

*Graduate Student, sc267@buffalo.edu.
†Assistant Professor, sonjoy@buffalo.edu.

several weeks or months to experimentally obtain a micro-structural image as shown, e.g., in Figure 2a. The macroscopic (continuum) material properties (in particular, constitutive elasticity tensors) are treated here as stochastic material properties to account for the effects of underlying micro-structural fluctuations since it is impractical and intractable to incorporate such effects deterministically for the entire structural system. The link between micro- and macro- scales are two matrix-valued bounds of the macroscopic constitutive elasticity tensor[6,7]. Let the matrix representation of the fourth-order macroscopic constitutive random elasticity tensor be denoted by $\mathbf{C}^{(M)}$, and its upper and lower bounds, respectively, by $C_u^{(M)}$ and $C_l^{(M)}$. These bounds can be calculated from deterministic micro-mechanical analyses of a small microscopic heterogeneous material volume element, $V^{(m)}$. Here, the superscripts, $^{(M)}$ and $^{(m)}$, imply association, respectively, with macro-scale and micro-scale. In the ensuing discussion, these superscripts, however, may be suppressed for the sake of simplified notations if no ambiguity exists. It will be evident from the context whether a variable under discussion is associated with the micro-scale or macro-scale. It can be shown that $\mathbf{C} \equiv \mathbf{C}^{(M)}$, in general (regardless of the fact whether $V^{(m)}$ contains any micro-cracks or not), satisfies the following[6,7],

$$C_l \leq \mathbf{C} \leq C_u \quad \text{a.s.} \tag{1}$$

Here, $C_l \equiv C_l^{(M)} \in \mathbb{M}_N^+(\mathbb{R})$ and $C_u \equiv C_u^{(M)} \in \mathbb{M}_N^+(\mathbb{R})$ are matrix-valued bounds, and $\mathbb{M}_N^+(\mathbb{R})$ represents the space of all $N \times N$ real symmetric and positive-definite matrices. Specific value of $N$ depends on the problem of interest. In eq. (1), the inequalities should be interpreted in the positive-definite sense (for instance, $C_l < \mathbf{C}$ implies that $(\mathbf{C} - C_l)$ is a positive-definite matrix a.s.), and a.s. (almost surely, i.e., with probability one) should be measured with respect to (w.r.t.) the joint probability measure of all the associated random variate(s) characterizing the uncertainties that, in the present work, model the effects of underlying micro-structural features.

It should be noted that if $V \equiv V^{(m)}$ contains any micro-cracks, then the resulting matrix-valued bounds, $C_l^{(d)} \equiv C_l^{(M,d)}$ and $C_u^{(d)} \equiv C_u^{(M,d)}$, are certainly different from the corresponding bounds, $C_l^{(h)} \equiv C_l^{(M,h)}$ and $C_u^{(h)} \equiv C_u^{(M,h)}$, obtained from $V$ without any micro-cracks. Under very general conditions (e.g., traction acting on the inner surface of micro-cracks is zero), it can be further shown that[7],

$$C_l^{(d)} < C_l^{(h)}, \text{ and } C_u^{(d)} < C_u^{(h)}, \tag{2}$$

where the inequalities must again be interpreted in the positive-definite sense. Eq. (2) shows remarkably strong theoretical results that clearly reflect the weakening effects of material stiffness because of the presence of micro-cracks. Finally, it should be noted that eq. (1) implies $\mathbf{S} = \mathbf{C}^{-1}$ is similarly bounded by $S_l = (C_u)^{-1}$ and $S_u = (C_l)^{-1}$, i.e., $S_l \leq \mathbf{S} \leq S_u$ a.s.[5]. Similar argument holds for eq. (2), i.e., $S_l^{(h)} < S_l^{(d)}$ and $S_u^{(h)} < S_u^{(d)}$.

By having recourse to the principle of maximum entropy (MaxEnt), the probability density function (pdf) of the matrix-variate random constitutive elasticity matrix, $\mathbf{C}$, is subsequently estimated[2,3]. While the pdf based on a healthy microscopic material volume element is supported over the set $\{C \in \mathbb{M}_N^+(\mathbb{R}) : C_l^{(h)} \leq C \leq C_u^{(h)}\}$, the pdf associated with a damaged microscopic material volume element containing micro-cracks is supported over $\{C \in \mathbb{M}_N^+(\mathbb{R}) : C_l^{(d)} \leq C \leq C_u^{(d)}\}$. Use of these pdfs produces significantly different probabilistic and statistical features for certain energy-based macroscopic response variables, thus reflecting the signatures of micro-anomalies in the underlying microstructures. The current work utilizes such apriori calibrated deterministic and heuristic information along with experimentally obtained information, within the scope of an optimization module, to detect the region of damage. To demonstrate this claim, an example problem to identify the signature of micro-cracks is presented in the current work. The relevant theory, numerical schemes, and results are presented in the following sections.

## II. Micro-mechanical analysis

The upper bound, $C_u$, is evaluated from the results of finite element (FE) analysis of $V$ subjected to kinematic uniform boundary condition (KUBC) given by $\mathbf{u}^{(m)}(\mathbf{x}) = \boldsymbol{\varepsilon}_o\,\mathbf{x}, \forall \mathbf{x} \in \partial V^{(m)}$, where $\partial V^{(m)}$ represents the boundary of $V$ and $\mathbf{u}^{(m)}(\mathbf{x})$ represents the prescribed displacement vector determined by

the values of a constant symmetric second-order strain tensor $\boldsymbol{\varepsilon}_o$. By abusing notation (for the sake of simplification of notation), we would, however, denote the vector-valued representation (Voigt notation) of $\boldsymbol{\varepsilon}_o$ also by $\boldsymbol{\varepsilon}_o$ in the following discussion. It will be clear from the context whether we are referring to the second-order strain tensor $\boldsymbol{\varepsilon}_o$ or its Voigt representation. It can be then derived that[6],

$$\langle \boldsymbol{\sigma}^{(m)} \rangle_V = C_u \, \boldsymbol{\varepsilon}_o, \tag{3}$$

in which $\boldsymbol{\sigma}^{(m)}(\mathbf{x})$ is the Voigt representation of the second-order tensor-valued stress field over $V$, and $\langle \cdot \rangle_V$, in the absence of micro-cracks, represents the volume average over $V$, for example,

$$\langle \boldsymbol{\sigma}^{(m)} \rangle_V := \frac{1}{V} \int_V \boldsymbol{\sigma}^{(m)}(\mathbf{x}) \, d\mathbf{x}$$

It can be further shown that[6],

$$\begin{aligned} \langle \phi^{(m)} \rangle_V &:= \frac{1}{V} \int_V \frac{1}{2} \left\{ \boldsymbol{\sigma}^{(m)}(\mathbf{x}) \right\}^T \boldsymbol{\varepsilon}^{(m)}(\mathbf{x}) \, d\mathbf{x} \\ &= \frac{1}{2} \langle \boldsymbol{\sigma}^{(m)} \rangle_V^T \, \boldsymbol{\varepsilon}_o = \frac{1}{2} \boldsymbol{\varepsilon}_o^T \, C_u \, \boldsymbol{\varepsilon}_o = \frac{1}{2} \langle \boldsymbol{\sigma}^{(m)} \rangle_V^T \, S_l \, \langle \boldsymbol{\sigma}^{(m)} \rangle_V \end{aligned} \tag{4}$$

where $\boldsymbol{\varepsilon}^{(m)}(\mathbf{x})$ is the Voigt representation of the second-order tensor-valued strain field over $V$.

The lower bound, $C_l$, is similarly evaluated from analysis of $V$ subjected to static uniform boundary condition (SUBC) such that the applied traction vector surface density, $\mathbf{t}^{(m)}(\mathbf{x})$, takes the following form, $\mathbf{t}^{(m)}(\mathbf{x}) = \boldsymbol{\sigma}_o \, \mathbf{n}(\mathbf{x}), \forall \mathbf{x} \in \partial V$. Here, $\boldsymbol{\sigma}_o$ is a constant symmetric stress matrix and $\mathbf{n}(\mathbf{x})$ denotes the unit vector normal to $\partial V \equiv \partial V^{(m)}$ at $\mathbf{x}$. In the following discussion, we would also use $\boldsymbol{\sigma}_o$ to denote the second-order stress tensor and its Voigt representation for notational simplicity. It can be then shown that[6],

$$\langle \boldsymbol{\varepsilon}^{(m)} \rangle_V = S_u \, \boldsymbol{\sigma}_o, \quad S_u = (C_l)^{-1} \tag{5}$$

$$\langle \phi^{(m)} \rangle_V = \frac{1}{2} \langle \boldsymbol{\varepsilon}^{(m)} \rangle_V^T \, \boldsymbol{\sigma}_o = \frac{1}{2} \boldsymbol{\sigma}_o^T \, S_u \, \boldsymbol{\sigma}_o = \frac{1}{2} \langle \boldsymbol{\varepsilon}^{(m)} \rangle_V^T \, C_l \, \langle \boldsymbol{\varepsilon}^{(m)} \rangle_V \tag{6}$$

In the presence of micro-cracks, the above discussion still holds theoretically provided the volume average stress and strain variables, $\langle \boldsymbol{\sigma}^{(m)} \rangle_V$ and $\langle \boldsymbol{\varepsilon}^{(m)} \rangle_V$, are appropriately re-defined[7].

The bounds, $C_l^{(h)}$, $C_u^{(h)}$, $C_l^{(d)}$, $C_u^{(d)}$, now can be calculated using the stress, strain and energy averages by solving four convex optimization problems in terms of their inverses (for better numerical conditioning) as shown below,

$$\begin{aligned} &\min_{S \in \mathbb{M}_N^+} \frac{\| (S \langle \boldsymbol{\sigma}^{(m)} \rangle) - \langle \boldsymbol{\varepsilon}^{(m)} \rangle \|_F}{\| \langle \boldsymbol{\varepsilon}^{(m)} \rangle \|_F} \\ &\text{s.t.} \left| \frac{0.5 \langle \boldsymbol{\sigma}^{(m)} \rangle^T \, S \, \langle \boldsymbol{\sigma}^{(m)} \rangle - \langle \phi^{(m)} \rangle}{\langle \phi^{(m)} \rangle} \right| < \epsilon \\ &\text{and suitable additional constraints (if any; see Table 1),} \end{aligned} \tag{7}$$

and then computing $C_l^{(h)}$, $C_u^{(h)}$, $C_l^{(d)}$, $C_u^{(d)}$ per last row of Table 1. Here, $\epsilon$ should be chosen a suitable small number (say, $1 \times 10^{-6}$). In the above formulation, the volume average notation is simplified by suppressing the subscript in $\langle \cdot \rangle_V$.

**Table 1. Additional constraints, and determination of bounds from their inverses.**

| Case | $S \equiv S_l^{(h)}$ | $S \equiv S_u^{(h)}$ | $S \equiv S_l^{(d)}$ | $S \equiv S_u^{(d)}$ |
|---|---|---|---|---|
| Additional constraints | None | $S - S_l^{(h)} \in \mathbb{M}_N^+$ | $S - S_l^{(h)} \in \mathbb{M}_N^+$ | $S - S_l^{(d)} \in \mathbb{M}_N^+$<br>$S - S_u^{(h)} \in \mathbb{M}_N^+$ |
| Output | $C_u^{(h)} = (S_l^{(h)})^{-1}$ | $C_l^{(h)} = (S_u^{(h)})^{-1}$ | $C_u^{(d)} = (S_l^{(d)})^{-1}$ | $C_l^{(d)} = (S_u^{(d)})^{-1}$ |

## III. Analysis of the macro-scale systems

In the absence of sufficient micro-structural information, it will be assumed here that the pdf, $p_{\mathbf{C}}(C)$, of $\mathbf{C}$ is uniformly distributed over $\mathcal{C} = \{C \in \mathbb{M}_N^+(\mathbb{R}) : C_l < C < C_u\}$. This is consistent with proposition of the MaxEnt principle, and will be practically useful if the 'gap' between $C_l$ and $C_u$ is small. It is earlier shown that such matrix-variate uniform distribution is a special case of generalized matrix-variate Beta type I distribution[3]. Let us denote the generalized matrix-variate Beta type I distribution parameterized by $a$, $b$, $C_u$, and $C_l$ as $GB_N^I(a, b; C_u, C_l)$. If $a = b = \frac{1}{2}(N+1)$, then $GB_N^I(a, b; C_u, C_l)$ turns out to be the matrix-variate uniform distribution supported over $\mathcal{C}$ and will be denoted by $\mathcal{U}_N(C_l, C_u)$. The sampling scheme to generate realizations of $\mathbf{C} \sim \mathcal{U}_N(C_l, C_u)$ is sketched in Figure 1[2]. Analysis of a macroscopic system can now be carried out in a Monte Carlo fashion by sampling $\mathbf{C}$ from $\mathcal{U}_N(C_l^{(h)}, C_u^{(h)})$ and $\mathcal{U}_N(C_l^{(d)}, C_u^{(d)})$ following certain damage initiation criteria as explained in Table 2. Although in this case the exceeding of a threshold Von Mises stress is assumed to be the criterion for initiation of damage, one may use any other general criteria of the form $\mathcal{F}(\boldsymbol{\sigma}, \boldsymbol{\varepsilon}, C, \mathbf{x}) \geq \mathcal{F}_{max}$, where $\mathcal{F}$ may be some functional which when exceeds some prescribed threshold value $\mathcal{F}_{max}$ damage initiation occurs at position $\mathbf{x}$.

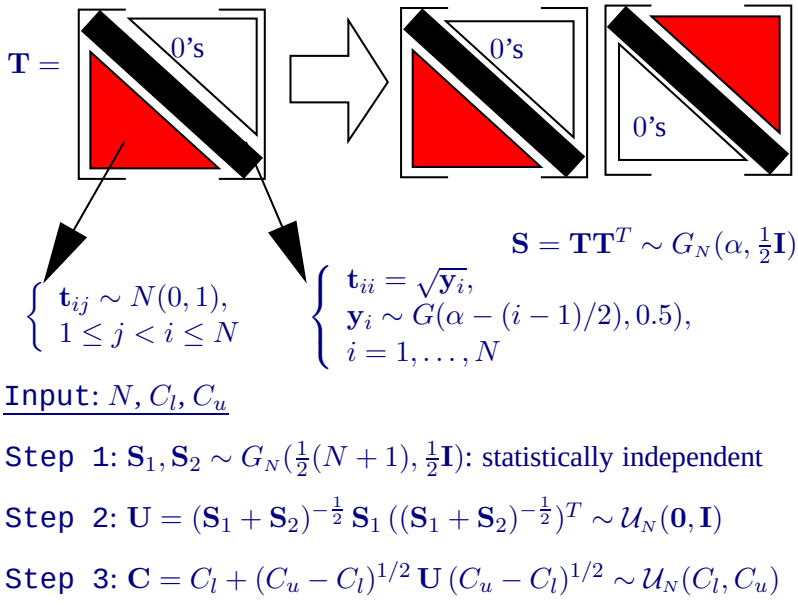


**Figure 1. Sampling from $\mathcal{U}_N(C_l, C_u)$**

**Table 2. Algorithm for macromechanical analysis using Monte Carlo simulation**

(1) Two populations of size $N_s$ generated for random matrices $\mathbf{C}^{(\mathbf{h})}$ and $\mathbf{C}^{(\mathbf{d})}$.
(2) Initialize realization counter: $j = 1$.
(3) For the $j$-th pair of realizations, $C_j^{(h)}, C_j^{(d)}$:
  (i) Initialize iteration counter $k = 1$, $s_i = 0$ for each FE node $i$ of given mesh $\mathcal{M}_{n,e}$
  (ii) If $s_i = 1$ then $C^{(i)} = C^{(d)}$, or else $C^{(i)} = C^{(h)}$.
  (iii) For any point $\mathbf{x}$, $C(\mathbf{x})$ is linearly interpolated from the nodal $C^{(i)}$'s of the element containing $\mathbf{x}$.
  (iv) FE problem, $[\mathbf{K}][\mathbf{U}] = [\mathbf{F}]$, is solved, where $[\mathbf{K}]$ is the global stiffness matrix, $[\mathbf{U}]$ is the nodal displacement vector and $[\mathbf{F}]$ is the nodal force vector.
  (v) Von Mises stress ${\sigma_{von}}^{(i)}$ evaluated at the nodes.
  (vi) If ${\sigma_{von}}^{(i)} \geq \sigma_{von}^o$, then set $s_i = 1$. Set $n_k =$ number of 0 to 1 transitions in set $\{s_i\}$.
  (vii) If $n_k = 0 \Rightarrow$ damage nucleation converges. Do $j = j + 1$ and go to (4).
    Or else: Do k=k+1 and continue from (3-ii).
(4) If $j <= N_s$ then continue from (3), or else go to (5).
(5) Postprocess to calculate and plot relevant statistics.

## IV. Detection of damage

The suggested numerical scheme to determine the region of damage are all based on an optimization problem where the objective is to minimize the difference between the observed strain $\boldsymbol{\varepsilon}^{(obsv)}$ and the modeled strain $\boldsymbol{\varepsilon}^{(modl)}$, with the decision variables being either the material points where the damage and healthy material properties are to be allocated, or the material properties themselves, or both. The degree of availability of information will determine which scheme among those suggested will give the best performance. For the purpose of optimization a fixed finite element (FE) mesh $\mathcal{M}_{(n_m,e_m)}$ with $n_m$ nodes and $e_m$ elements is chosen. The current discussion will use the definitions given in Table 3.

**Table 3. Terminology used in the damage detection scheme(s)**

| | |
|---|---|
| $\left(C^{(h,x)}, C^{(d,x)}\right)$ | Material properties used to create the actual observation $(x = true)$ and predicted by the optimization module $(x = modl)$, respectively. |
| $\boldsymbol{\varepsilon}^{(obsv,i)}$ | Observed strain field of the $i$-th node of mesh $\mathcal{M}_{n_m,e_m}$ which is determined by first simulating the damage evolution scheme using $C^{(h,true)}, C^{(d,true)}$ on a very fine mesh $(\mathcal{M}_{n_o,e_o} : n_o >> n_m, e_o >> e_m)$, followed by interpolation of the observed field, strain in this case, to the nodes of mesh $\mathcal{M}_{n_m,e_m}$. |
| $P^{(i)}$ | Probability of damage at the i-th node. This is determined from the Monte Carlo simulation with $N_s$ randomly generated material samples $(\mathbf{C}^{(h)}, \mathbf{C}^{(d)})$ each of which is used to emulate the damage evolution on a relatively finer mesh $(\mathcal{M}_{n_p,e_p} : n_o > n_p > n_m, e_o > e_p > e_m)$. The field $P$ is evaluated on $\mathcal{M}_{n_p,e_p}$ and then interpolated to the nodes of $\mathcal{M}_{n_m,e_m}$. Unless otherwise specified, both the $C^{(h,true)}, C^{(d,true)}$ and random matrix samples $(\mathbf{C}^{(h)}, \mathbf{C}^{(d)})$ (used to calibrate $P^{(i)}$) correspond to the same microstructure, implying that they both have the same stiffness matrix bounds $\{C_l^{(h)}, C_u^{(h)}, C_l^{(h)}, C_u^{(d)}\}$. |
| $\phi^{(x,i)}$ | Energy density at node $i$ of $\mathcal{M}_{(n_m,e_m)}$ defined in Equation(8). In this definition constitutive matrix, $C$, and the strain vector, $\boldsymbol{\varepsilon}$, are expressed in Voigt notation. |
| $e_I^{(i)}, e_{II}^{(i)}$ | Relative and absolute errors in modeling nodal energy density at node $i$ of $\mathcal{M}_{(n_m,e_m)}$ defined in Equations (9) and (10). |
| $U^{(h)}, U^{(d)}, U^{(i)}$ | These are matrices that lie between $\mathbf{0}$ and $\mathbf{I}$ in the positive definite sense and are used to determine $\{C^{(h,modl)}, C^{(d,modl)}\}$ and $\{C^{(h,modl,i)}, C^{(d,modl,i)}\}$, respectively, based on the Equations (11), (12), (13) and (14). |
| $s_i$ | Damage flag at node $i$ of $\mathcal{M}_{(n_m,e_m)}$ which takes value 0 when the node is allocated healthy material property $C^{(i)} = C^{(h)}$ and 1 when the node is allocated damaged material property $C^{(i)} = C^{(d)}$. |
| $\mathcal{N}_0, \mathcal{N}_1, \mathcal{N}_k, \mathcal{N}_l, \mathcal{N}_f$ | Prospective search spaces for optimization which are defined in Equations (15), (16), (19) and (20). Region $\mathcal{N}_f$ is created using algorithm given in Table 4. In these definitions, the term $\theta_k$ and $\theta_l$ are fractions used to set thresholds for creating the subspaces $\mathcal{N}_k$ and $\mathcal{N}_l$, respectively, the term $L_{\max}$ is the maximum edge length of the smallest rectangle enclosing the geometry and the term $\theta_P$ is a user-defined fraction to prescribe the nodal space to search. Thus $L_{\max}\theta_P$ can be used to define a neighborhood around the region corresponding to nonzero probability of damage. The set $\mathcal{N}_f$ is the region that includes the nodes comprising the boundary of the damaged region and $N_{lmax}$ number of node layers away from these boundary nodes going into the healthy region. |
| $f_{n\to e}(\cdot)$ | Function that takes in a set of FE node labels as argument and returns the set of element labels each of which has atleast one node that is common to the prescribed node set. |
| $f_{e\to n}(\cdot)$ | Function that takes in a set of finite element labels as argument and returns the set of node labels connected to all these elements. |

$$\phi^{(x,i)} = 0.5 \left[\boldsymbol{\varepsilon}^{(x,i)}\right]^T C^{(i)} \left[\boldsymbol{\varepsilon}^{(x,i)}\right] : x \in \{obsv, modl\} \tag{8}$$

$$e_I^{(i)} = ((\phi^{(modl,i)} - \phi^{(obsv,i)})/\phi^{(obsv,i)})^2 \tag{9}$$

$$e_{II}^{(i)} = (\phi^{(modl,i)} - \phi^{(obsv,i)})^2 \tag{10}$$

$$C^{(h,modl)} = C_l^{(h)} + (C_u^{(h)} - C_l^{(h)})^{1/2} U^{(h)} (C_u^{(h)} - C_l^{(h)})^{1/2} \tag{11}$$

$$C^{(d,modl)} = C_l^{(d)} + (C_u^{(d)} - C_l^{(d)})^{1/2} U^{(d)} (C_u^{(d)} - C_l^{(d)})^{1/2} \tag{12}$$

$$C^{(h,modl,i)} = C_l^{(h)} + (C_u^{(h)} - C_l^{(h)})^{1/2} U^{(i)} (C_u^{(h)} - C_l^{(h)})^{1/2} \tag{13}$$

$$C^{(d,modl,i)} = C_l^{(d)} + (C_u^{(d)} - C_l^{(d)})^{1/2} U^{(i)} (C_u^{(d)} - C_l^{(d)})^{1/2} \tag{14}$$

$$\mathcal{N}_0 = \{1, \cdots, n_m\} \tag{15}$$

$$\mathcal{N}_1 = \left\{ i : \|\mathbf{x}^{(i)} - \mathbf{x}^{(j)}\|^{\frac{1}{2}} < L_{\max} \theta_P \forall i \in \mathcal{N}_0, j \in \mathcal{N}_P \right\} \tag{16}$$

$$\mathcal{N}_P = \left\{ k : P^{(k)} \neq 0 \forall k \in \mathcal{N}_0 \right\} \tag{17}$$

$$\mathcal{N}_0 \Rightarrow \mathcal{N} = \left\{ i_1, \cdots, i_{n_m} : e_I^{(i_j)} \geq e_I^{(i_{j+1})} \forall j \in \{1, \cdots, (n_m - 1)\} \right\} \tag{18}$$

$$\mathcal{N}_k = \{i_1, \cdots, i_k\} : \sum_{k \in \mathcal{N}_k} e_I^{(k)} = \theta_k \sum_{i=1}^{n_m} e_I^{(i)} \tag{19}$$

$$\mathcal{N}_l = \{i_{k+1}, \cdots, i_l\} : \sum_{l \in \mathcal{N}_l} e_I^{(l)} = \theta_l \sum_{i=1}^{n_m} e_I^{(i)} \tag{20}$$

**Table 4. Algorithm for determination of region $\mathcal{N}_f$**

| | |
|---|---|
| Initialization: | $\begin{cases} \mathcal{N}_d = \{k : s_k = 1 \forall k \in \mathcal{N}_0\}; \mathcal{N}_h = \mathcal{N}_0 - \mathcal{N}_d; \mathcal{E}_d = f_{n \to e}(\mathcal{N}_d); \mathcal{E}_h = f_{n \to e}(\mathcal{N}_h); \mathcal{E}_{dh} = \mathcal{E}_h \cap \mathcal{E}_d; \\ \mathcal{N}_l^{(1)} = f_{e \to n}(\mathcal{E}_{dh}); \mathcal{N}_l^{(1)} = \mathcal{N}_l^{(1)} \cap \mathcal{N}_d; \mathcal{E}_l^{(1)} = f_{n \to e}(\mathcal{N}_l^{(1)}); \mathcal{N}_{all}^{(1)} = \mathcal{N}_l^{(1)} \cup \mathcal{N}_d; \mathcal{N}_f = \mathcal{N}_l^{(1)}; \end{cases}$ |
| Iteration: | for $j = (2 \text{ to } 1 + N_{lmax})$ do: |
| | $\begin{cases} \mathcal{N}_l^{(j)} = f_{e \to n}(\mathcal{E}_l^{(j-1)}); \\ \mathcal{N}_l^{(j)} = \left(\mathcal{N}_l^{(j)} \cup \mathcal{N}_{all}^{(j-1)}\right) - \mathcal{N}_{all}^{(j-1)}; \\ \mathcal{E}_l^{(j)} = f_{n \to e}(\mathcal{N}_l^{(j)}); \\ \mathcal{N}_{all}^{(j)} = \mathcal{N}_l^{(j)} \cup \mathcal{N}_{all}^{(j-1)}; \\ \mathcal{N}_f = \mathcal{N}_f \cup \mathcal{N}_l^{(j)}; \end{cases}$ |

Three different scenarios of increasing challenge and the corresponding optimization schemes are suggested in Table 5. The optimization problem(s) are posed in Table 6. The primary goal is to determine the optimum damage flag vector $\mathcal{S} = \left[s^{(i)}\right]$ such that the corresponding modeled strain matches the observed strain as best as possible. In scenario 2 and 3, a secondary goal is adopted which is to determine the optimum material parameters $\mathcal{C} = \left[C^{(i)}\right]$, the constitutive matrices allocated to FE nodes, so as to complement the primary goal. The material parameters are determined from the decision variable $U$ using Equations (11), (12), (13) and (14). It is important to note that in the multistage optimization schemes, between any two successive optimization stages, the optimal solution from the previous stage is passed on as one of the initial guesses for the following stage, thus with each stage the quality of solution improves. The multistage region optimization scheme, $\mathcal{O}_1$, is an integer optimization problem for which the solution procedure adopted is a simple Binary encoded Genetic Algorithm (BGA). The multistage material parameter optimization, $\mathcal{O}_2$,

is solved using a Real encoded Genetic Algorithm (RGA). By virtue of its strengths as a global optimizer and no requirement on gradient based information, Genetic Algorithm[4] is deemed suitable for $\mathcal{O}_1$ and $\mathcal{O}_2$, both of which work on search spaces of high dimension. The single stage material parameter optimization scheme, $\mathcal{O}_3$, is solved using a traditional gradient based optimization technique, e.g. Interior point method[1], but with multiple initial guesses such that the best among these independently derived prospective optima is chosen as the desired optimum. In all these scenarios it will be implied that the mesh $\mathcal{M}_{n_m,e_m}$, boundary conditions and external loading (known apriori) will be used, in conjunction with each set of prospective optimal parameters from the optimization problem and other known information, to solve a FE problem and subsequently evaluate the objective function.

**Table 5. Different scenarios classified based on the availability of information**

| # | **Known information** | **Unknown** | **Scheme** |
|---|---|---|---|
| 1 | $\{\boldsymbol{\varepsilon}^{(obsv,i)}, C^{(h,true)}, C^{(d,true)}, P^{(i)}\}$. | $\{\mathcal{S}\} : s_i = 0 \Rightarrow C^{(i)} = C^{(h,true)}; s_i = 1 \Rightarrow C^{(i)} = C^{(d,true)}$. | $\mathcal{O}_1$ |
| 2 | $\{\boldsymbol{\varepsilon}^{(obsv,i)}, C_l^{(h)}, C_u^{(h)}, C_l^{(d)}, C_u^{(d)}, P^{(i)}\}$. | $\{\mathcal{S}, U^{(h)}, U^{(d)}\} : s_i = 0 \Rightarrow C^{(i)} = C^{(h,modl)}; s_i = 1 \Rightarrow C^{(i)} = C^{(d,modl)}$. | $\mathcal{O}_1 \rightarrow \mathcal{O}_3 \rightarrow \mathcal{O}_1$ |
| 3 | $\{\boldsymbol{\varepsilon}^{(obsv,i)}, C_l^{(h)}, C_u^{(h)}, C_l^{(d)}, C_u^{(d)}, P^{(i)}\}$. Here the material bounds may not always correspond to the actual microstructure for which the observation is evaluated. | $\{\mathcal{S}, U^{(h,i)}, U^{(d,i)}\} : s_i = 0 \Rightarrow C^{(i)} = C^{(h,modl,i)}; s_i = 1 \Rightarrow C^{(i)} = C^{(d,modl,i)}$. | $\mathcal{O}_1 \rightarrow \mathcal{O}_2 \rightarrow \mathcal{O}_1$ |

**Table 6. Single and multi-stage schemes for region and material parameter optimization**

| Stage # | Multistage region optimization $\mathcal{O}_1$ | Stage # | Multistage parameter optimization $\mathcal{O}_2$ |
|---|---|---|---|
| 1 | $\min_{S\in\{0,1\}^{\lvert\mathcal{N}_1\rvert}, S\subseteq\mathcal{S}} e(S) = \sum_{i\in\{\mathcal{N}_1\}} e_I^{(i)}$ | 1 | $\min_{U=\{U^{(j)}:\mathbf{0}\le U^{(j)}\le\mathbf{I}\forall j\in\mathcal{N}_0\}} e(U) = \sum_{i\in\{\mathcal{N}_1\}} e_I^{(i)}$ |
| 2 | $\min_{S\in\{0,1\}^{\lvert\mathcal{N}_k\rvert}, S\subset\mathcal{S}} e(S) = \sum_{i\in\{\mathcal{N}_k\}} e_I^{(i)}$ | 2 | $\min_{U=\{U^{(j)}:\mathbf{0}\le U^{(j)}\le\mathbf{I}\forall j\in\mathcal{N}_k\}} e(U) = \sum_{i\in\{\mathcal{N}_k\}} e_I^{(i)}$ |
| 3 | $\min_{S\in\{0,1\}^{\lvert\mathcal{N}_l\rvert}, S\subset\mathcal{S}} e(S) = \sum_{i\in\{\mathcal{N}_l\}} e_I^{(i)}$ | 3 | $\min_{U=\{U^{(j)}:\mathbf{0}\le U^{(j)}\le\mathbf{I}\forall j\in\mathcal{N}_l\}} e(U) = \sum_{i\in\{\mathcal{N}_l\}} e_I^{(i)}$ |
| 4 | $\min_{S\in\{0,1\}^{\lvert\mathcal{N}_f\rvert}, S\subset\mathcal{S}} e(S) = \sum_{i\in\{\mathcal{N}_f\}} e_I^{(i)}$ | 4 | $\min_{U=\{U^{(j)}:\mathbf{0}\le U^{(j)}\le\mathbf{I}\forall j\in\mathcal{N}_f\}} e(U) = \sum_{i\in\{\mathcal{N}_f\}} e_I^{(i)}$ |
| 5 | $\min_{S\in\{0,1\}^{\lvert\mathcal{N}_f\rvert}, S\subset\mathcal{S}} e(S) = \sum_{i\in\{\mathcal{N}_f\}} e_{II}^{(i)}$ | 5 | $\min_{U=\{U^{(j)}:\mathbf{0}\le U^{(j)}\le\mathbf{I}\forall j\in\mathcal{N}_f\}} e(U) = \sum_{i\in\{\mathcal{N}_f\}} e_{II}^{(i)}$ |
| Single stage parameter optimization $\mathcal{O}_3$ | | | |
| $\min_{U=\{U^{(h)},U^{(d)}:\mathbf{0}\le U^{(h)},U^{(d)}\le\mathbf{I}\}} e(U) = \sum_{i\in\{\mathcal{N}_1\}} e_I^{(i)}$ | | | |

## V. Numerical Implementation

The proposed approach will be illustrated by considering computer simulated micro-structures of Aluminium based material (see Figure 2) and a macroscopic model of an aircraft wing subjected to body force, $\mathbf{b}_F$. The following numerical results are based on the micro-structures shown in Figure 2c. Plane stress formulation of adaptive FE scheme with 3-noded constant stress triangular elements is adopted to carry out both the micro-mechanical and macroscopic analyses.Based on $N = 1000$ realizations of the aircraft wing, the probability of presence of micro-cracks is reported in Figure 3. Finally, pdfs of certain energy-based macroscopic response variables, $\phi$ at $(x, y) = (6, 3.5)$ m are also shown in Figure 4 that clearly displays distinct probabilistic features for healthy microstructures (Figure 2a) and that of damaged microstructures (Figure 2c). This finding can be readily used to capture the signatures of micro-cracks with high probability. A new realization of $\phi$, that was not used in the Monte Carlo analysis to estimate the probability plots (Figure 3) and pdfs (Figure 4), is also in shown Figure 4. The new realization is found to belong to the support of pdf $p_{\boldsymbol{\phi}}$, which provides some evidence of numerical cross-validation in support of the proposed approach.

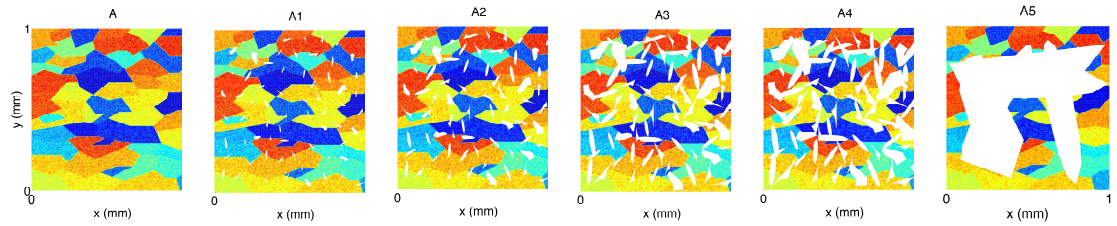


(a) (b) (c) (d) (e) (f)

**Figure 2. Illustrations of micro-structural images with increasing damage levels (starting with no micro-cracks at the left most image); different colors indicate different material properties of grains; white color represents openings due to micro-cracks.**

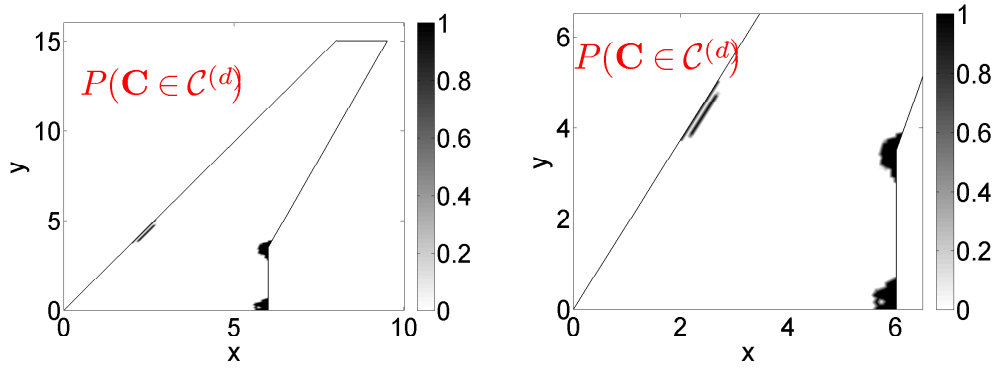


(a) (b)

**Figure 3. (a) Probability of presence of micro-cracks, (b) zoomed view.**

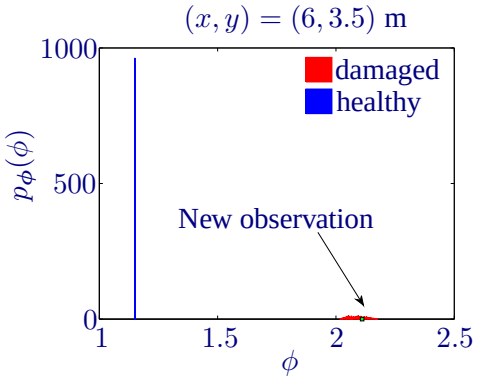


**Figure 4. pdf of energy-based macroscopic response variable show distinct features for healthy and damaged microstructures.**

Next we demonstrate the capability of detection of micro-cracks in the macrostructure based on a limited selection of available information for the different scenarios described above. The algorithms are encoded in `MATLAB(R2012a)` and executed on a parallel computing cluster. For the FEA evaluation, required both in the calibration and the optimization phases, Matlab's `PDE Toolbox` is found to be useful. For the optimization Matlab's `Global Optimization Toolbox` is used for genetic algorithm based and gradient-based traditional optimization. Matlab's inbuilt parallel and distributed computing capability has been utilized in the current study. A coarse mesh $\mathcal{M}(n_m = 2147, e_m = 4060)$ comprising of plane stress triangular elements is created apriori for the purpose of optimization. The coarse mesh used in optimization makes the detection process faster. The important optimization parameters that need to be specified are: population size $(n_{pop})$ in GA, maximum number of generations for GA $(gen_{max})$, probability of crossover for GA $(P_c)$, probability of mutation for GA $(P_m)$, number of elite chromosomes to be preserved across generations in GA $(n_{elite})$, function tolerance for convergence $(\epsilon_F)$, tolerance on nonlinear constraints $(\epsilon_{con})$ to check constraint feasibility, tolerance on decision variable for convergence $(\epsilon_X)$ and minimum change for decision variable for finite difference calculation $(\delta X_{min})$. The number of processors used for distributed computing $(n_{proc})$ is also prescribed.

In Figure 5 we illustrate the performance of the optimization algorithm for Scenario 1. The results presented in the figure correspond to the final optimal solution after stage 5 in $\mathcal{O}_1$ has converged (see Table 5 and 6). In Figure 5(a) the probability contour obtained from much smaller sample size ($N_s = 25$) is used to generate the initial guess resulting in faster calibration. It is observed in the current study that

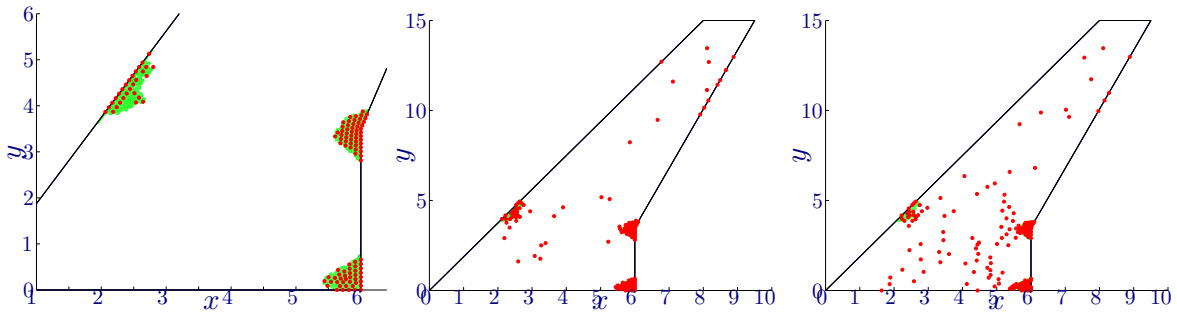


**Figure 5. Scenario 1: Initial guess for $S$ is generated based (a) $P^{(i)}$ (b) $\varepsilon^{(obsv)}$ (c) neither $P^{(i)}$ nor $\varepsilon^{(obsv)}$. Green patches depict the actual damaged region while the red dots refer to the FE nodes which are deemed damaged. BGA parameters for $\mathcal{O}_1$: $n_{pop} = 150, \epsilon_F = 10^{-8}, gen_{max} = 500, P_c = 0.9, P_m = 0.05, n_{elite}, = 1, \theta_P = 0.1, \theta_k = 0.9, \theta_l = 0.99, N_{lmax} = 1, n_{proc} = 12$. Cputime: (a) 0.51 hours (includes calibration overhead of 0.27 hours based $N_s = 25$ samples) (b) 0.61 hours (c) 0.58 hours.**

.
probability contour obtained $N_s = 25$ samples differs from that obtained from $N_s = 1000$ samples by less than $1\%$, hence deemed acceptable. A node with a higher value of $P^{(i)}$ has a higher chance of being damaged $\Rightarrow s_i = 1$. In Figure 5(b) the observed nodal strain is used to generate the initial guess. A node with a higher value of $\|\epsilon_{11}, \epsilon_{22}, 2\epsilon_{12}\|_2$ has a higher probability of being damaged $\Rightarrow s_i = 1$. In Figure 5(c) neither of the above two schemes are used and initial guess is generated randomly, thus each node has an equal chance of being either damaged or healthy. It can be noted that the final result is sensitive to the initial guess, and the information $P^{(i)}$ provides a marked advantage over the other two schemes in terms of cputime and quality of final solution using identical computational resources. This emphasizes the importance of the Monte Carlo simulation that results in the probability contour.

For scenario 2, a similar result is shown in Figure 6. In case of scenarios 2 and 3, the predicted damaged region presented in the results correspond to the final optimal solutions after stage 5, in the second instance of $\mathcal{O}_1$, has converged (see Table 5 and 6) in the respective cases. The optimal material parameters resulting after the single stage optimization $\mathcal{O}_3$ converges is given in Equation (21) and (22).

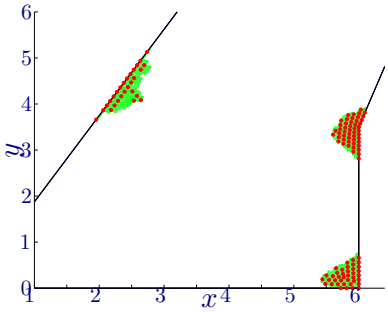

**Figure 6. Green patch depicts the actual damaged region while the red dots refer to the damaged FE nodes. BGA parameters for $\mathcal{O}_1$: $n_{pop} = 150, \epsilon_F = 10^{-8}, gen_{max} = 500, P_c = 0.9, P_m = 0.05, n_{elite}, = 1, \theta_P = 0.1, \theta_k = 0.9, \theta_l = 0.99, N_{lmax} = 1, n_{proc} = 12$. Interior point algorithm parameters for $\mathcal{O}_3$: 25 initial guesses, $\epsilon_F = 10^{-6}, \epsilon_{con} = 10^{-6}, \epsilon_X = 10^{-6}, \delta X_{min} = 10^{-7}$, Maximum function evaluation $= 10000$, Maximum iterations $= 3000, \theta_P = 0.1, n_{proc} = 12$,. cputime: 2.04 hours (includes calibration overhead)**

$$C^{(h,true)} = \begin{bmatrix} 80.0875 & 26.3163 & 0.0076 \\ 26.3163 & 79.7559 & -0.0485 \\ 0.0076 & -0.0485 & 26.7568 \end{bmatrix} \text{GPa}; C^{(h,modl)} = \begin{bmatrix} 79.9909 & 26.3664 & 0.0085 \\ 26.3664 & 79.8234 & -0.0294 \\ 0.0085 & -0.0294 & 26.7900 \end{bmatrix} \text{GPa} \quad (21)$$

$$C^{(d,true)} = \begin{bmatrix} 37.1816 & 8.9989 & 0.6823 \\ 8.9989 & 45.7229 & 0.1638 \\ 0.6823 & 0.1638 & 15.5409 \end{bmatrix} \text{GPa}; C^{(d,modl)} = \begin{bmatrix} 36.4222 & 10.2879 & 0.5209 \\ 10.2879 & 46.6090 & 0.3231 \\ 0.5209 & 0.3231 & 15.8933 \end{bmatrix} \text{GPa} \quad (22)$$

Finally, in Figure 7, we present the results for Scenario 3 for two cases: (a) when the observation is from

a material with the same microstructure corresponding to Figure 2c (hence, identical constitutive matrix bounds) as that used in the calibration and optimization (the same holds true for Scenario 1 and 2), and (b) when the observation is from a material with a different microstructure (Figure 2b, void fraction=$3.2\%$) w.r.t. that used in the calibration and optimization (Figure 2c, void fraction=$8.8\%$); the latter case is a more realistic situation. It can be noted that even for a different microstructure which has microcracks that make up a void volume fraction which is as low as $\sim 3\%$ in a $1mm \times 1mm$ square area, the algorithm is able to detect the region of damage based on its macrolevel strain response.

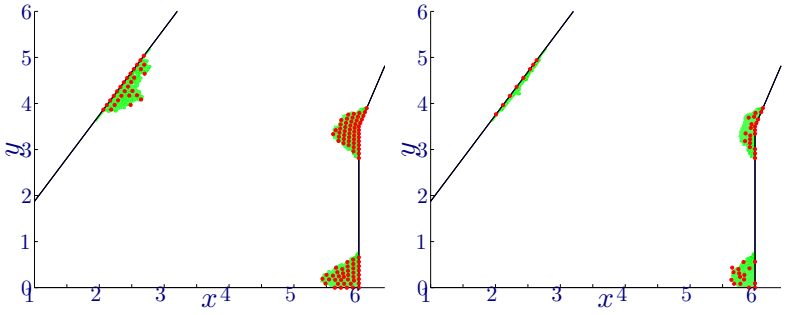


**Figure 7. Green patch depicts the actual damaged region while the red dots refer to the FE nodes which are deemed damaged by the detection module. (a) $\varepsilon^{(obsv)}$ corresponds to the microstructure shown in Figure 2c (b) $\varepsilon^{(obsv)}$ corresponds to the microstructure shown in Figure 2b. BGA parameters for $\mathcal{O}_1$: $n_{pop} = 150, \epsilon_F = 10^{-8}, gen_{max} = 500, P_c = 0.9, P_m = 0.05, n_{elite} = 1, P_c = 0.9, P_m = 0.05, n_{elite}, = 1, \theta_P = 0.1, \theta_k = 0.9, \theta_l = 0.99, N_{lmax} = 1, n_{proc} = 12$. RGA parameters for $\mathcal{O}_1$: $n_{pop} = 150, \epsilon_F = 10^{-8}, \epsilon_{con} = 10^{-8}, gen_{max} = 500, P_c = 0.9, P_m = 0.05, n_{elite}, = 1, \theta_P = 0.1, \theta_k = 0.9, \theta_l = 0.99, N_{lmax} = 1, n_{proc} = 12$. CPU time: (a) 1.57 hours (b) 1.65 hours (Calibration overhead included for both cases)**

## VI. Conclusion

In this current study we have presented and validated a generic methodology to detect microcrack from macrolevel responses. The generic nature of the suggested techniques adds to their robustness, thus they can be extended to detect any other kind of microanomaly. The detection methodology is primarily an optimization module which attempts to match the predicted model to the observed reality. It is also observed that the optimization module is quite sensitive to the quality of its initial condition, and to gain in efficiency in terms of both speed of computation and quality of results, a physics based initial guess provides the required means. With the argument in favor of such a preprocessing, one may appreciate the significance of microscale analysis in determining the constitutive matrix bounds and the macroscale analysis, based on random matrix theory and Monte Carlo simulation, in calibrating the probability contour which is consequently used in generation of initial guess for optimization. The current research work, which is a result of a confluence of mechanics, probability theory and optimization, may provide an efficient and robust tool in structural health monitoring and damage detection.

## References


[1]J.F. Bonnans, J.C. Gilbert, C. Lemaréchal, and C.A. Sagastizábal. *Numerical optimization: theoretical and practical aspects*. Universitext. Springer, 2 edition, 2006.

[2]S. Das and R. Ghanem. A bounded random matrix approach for stochastic upscaling. *Multiscale Model Simul.*, 8(1):296–325, 2009.

[3]S. Das and R. Ghanem. Stochastic upscaling for inelastic material behavior from limited experimental data. In Somnath Ghosh and Dennis Dimiduk, editors, *Computational Methods for Microstructure-Property Relationships*, pages 443–468. Springer, New York, 2011.

[4]D.E. Goldberg. *Genetic algorithms in search, optimization and machine learning*. Addison-Wesley Professional, 1 edition, 1989.

[5]R.A. Horn and C.R. Johnson. *Matrix Analysis*. Cambridge University Press, 1985.

[6]C. Huet. Application of variational concepts to size effects in elastic heterogeneous bodies. *J. Mech. Phys. Solids*, 38(6):813–841, 1990.

[7]C. Huet. An integrated micromechanics and statistical continuum thermodynamics approach for studying the fracture behaviour of microcracked heterogeneous materials with delayed response. *Engineering Fracture Mechanics*, 58(5-6):459–556, 1997.